東北大学機関リポジトリ
TOUR
Tohoku University Repository

Magnetic anisotropy and rotational hysteresis loss in exchange coupled Ni-Fe/Mn-Ir films

Magnetic anisotropy and rotational hysteresis loss in exchange coupled Ni−Fe/Mn−Ir films

Masakiyo Tsunoda,[a)] Yoshihiro Tsuchiya, Takahiko Hashimoto, and Migaku Takahashi
Department of Electronic Engineering, Tohoku University, Sendai 980-8579, Japan

The magnetic anisotropy and rotational hysteresis loss in Ni−Fe/Mn−Ir bilayers were investigated for films prepared by an ultraclean sputtering deposition process. An in-plane field of 30 Oe during deposition served to define the antiferromagnetic (AF) alignment axis for the Mn−Ir layer. The Ni−Fe layer thickness was maintained at 50 Å and the Mn−Ir layer thickness ranged from 20 to 200 Å. Room temperature magnetization and torque measurements were made as a function of the Mn−Ir layer thickness d_{AF} and the applied field. The magnetization data were obtained for fields applied in the same direction as during deposition. The magnetization data indicate a critical d_{AF} value of 37 Å, taken as d_{AF}^{cr}. For $d_{AF} > d_{AF}^{cr}$, the data show hysteresis loops which are displaced along the field axis. The torque response and rotational hysteresis characteristics are sensitive to both d_{AF} and the measuring field. (1) When d_{AF} is much less than d_{AF}^{cr}, the torque curves have a $\sin\theta$ characteristic at fields below 30–40 Oe or so which suddenly changes to a $\sin 2\theta$ characteristic at higher fields. With the onset of the $\sin 2\theta$ torque response, rotational hysteresis loss also appears but then vanishes for fields above 100 Oe or so. (2) As d_{AF} approaches d_{AF}^{cr} from below, the torque response is the same as above. Here, however, the rotational hysteresis appears for fields well below the field at which the torque response assumes a $\sin 2\theta$ character and persists to the maximum available measuring field of 15 kOe or so. (3) When d_{AF} exceeds d_{AF}^{cr}, the torque has a predominant $\sin\theta$ character at all fields and a small $\sin 2\theta$ component and rotational hysteresis which only around a field of 400 Oe or so. These results, while somewhat complicated, are in accord with responses evaluated from the simple exchange anisotropy model of W. H. Meiklejohn and C. P. Bean [Phys. Rev. **102**, 1413 (1956); **105**, 904 (1957)]. Among other things, one may conclude that a rotational hysteresis which persists to high field is not intrinsic to exchange anisotropy. © *2000 American Institute of Physics.* [S0021-8979(00)04609-0]

I. INTRODUCTION

The exchange biasing of a ferromagnetic (F) layer by an adjacent antiferromagnetic (AF) layer[1] is one of the key effects in the development of spin valve heads[2] for magnetic recording. Through such exchange biasing, the exchange coupling across the interface between the AF layer and the F layer effectively pins the magnetization direction on the F layer. A second F layer, separated from the first by a thin nonmagnetic (NM) layer, is free to respond to the magnetic field from the magnetic bits in the storage medium. There is a large change in the electrical resistance, the so-called giant magnetoresistance, of the F-NM-F sandwich as the magnetization direction in the free F layer changes relative to the pinned magnetization in the exchange coupled layer. This change yields the desired bit readout signal.

In spite of the intense interest in exchange biasing,[3] the detailed microscopic origins of this important effect remain unresolved.[4,5] The basic model for the effect is the exchange anisotropy model proposed by Meiklejohn and Bean (MB).[3,6] In this MB model, the F-AF interaction leads to the appearance of a unidirectional anisotropy with two characteristic manifestations. First, magnetization curves for fields applied parallel to the spin alignment axis in the AF layer are dis-

placed along the field axis, relative to the usual symmetric hysteresis loop for a ferromagnet. Second, curves of the torque versus the in-plane field angle θ relative to the unidirectional axis develop a unidirectional $\sin\theta$ character. These torque curves may also show rotational hysteresis loss, manifested by torque curves which are not completely reversible, but such losses vanish at high field, according to the model.

Experimental data on real F-AF systems, bulk as well as thin film, show these basic responses, but often with one crucial complication—a rotational hysteresis loss which persists to high field.[3,6–11] Many possible origins of this discrepancy have been proposed. These include various domain wall configurations in the AF or the F layer,[6] a more complex magnetization process in the F layer,[8] and direct interaction between the antiferromagnetic spins and the external applied field.[10] In spite of such proposals, however, there is still no clear physical model to explain these effects. The most reasonable element of the proposed models is some sort of inhomogeneity which results in a variation in the local F-AF exchange coupling and produces a coexistence of blockable and unblockable regions.[9] It was recently proposed that for thin films structures, such a situation could result from inhomogeneous microstructure for the antiferromagnetic layer.[12]

Previous work by the present authors has shown that film fabrication under a highly purified sputtering atmo-

---

a)Electronic mail: tsunoda@ecei.tohoku.ac.jp

sphere can lead to a significantly improved film morphology.[13,14] The data in Ref. 13, for example, show that Ni–Fe films fabricated under such conditions have an increased in-plane grain size and highly coherent (111) crystal planes with an extremely low fault density from the initial atomic layer to the top atomic layer of the film. Reference 14 shows that an antiferromagnetic film which is deposited directly on this Ni–Fe film under the same conditions will replicate the large grain and highly coherent microstructure of the Ni–Fe underlayer. The use of a highly purified and ultraclean sputtering process, therefore, should result in the realization of antiferromagnetic layers with a very homogeneous microstructure.

The present study focuses on the ferromagnetic-antiferromagnetic Ni–Fe/Mn–Ir film system.[15] Bilayers made up of 50 Å thick ferromagnetic Ni–Fe films and antiferromagnetic Mn–Ir films of different thicknesses were fabricated through the ultraclean sputtering process cited above. The aim was (1) to produce sandwich films with an enhanced structural homogeneity for the antiferromagnetic layer and (2) to use such films to study the fundamental exchange anisotropy process without the complications of an inhomogeneous microstructure. These bilayer films were used to measure magnetization versus field and torque versus in-plane field angle as a function of the Mn–Ir layer thickness and the applied field. These data were then used to determine (a) the film coercive force and exchange anisotropy field versus the Mn–Ir film thickness d_{AF}, and (b) the uniaxial and unidirectional torque response and the rotational hysteresis loss versus d_{AF} and the applied field used for the torque measurements. These experimental results were then compared with corresponding computations based on the original Meiklejohn and Bean (MB) model.

The details of the experiment and the calculations are presented below. Section II gives the procedures for the computations and the sample preparation and measurements. Section III gives the results of the model calculations and the measurements. Section III also provides a critical comparison of the model calculations with the data. Section IV considers various points of disagreement between the model and the measurements. Section V presents a summary and conclusion. The basic conclusions are easily stated. First, Ni–Fe/Mn–Ir bilayers fabricated under the ultraclean sputtering process have magnetic properties which typify exchange anisotropy interactions with minimal complications. Second, the data can be modeled through the Meiklejohn and Bean model with no major additional modifications.

II. PROCEDURE

A. Model for calculation

The model described below follows the basic exchange anisotropy concept developed by Meiklejohn and Bean.[3,6] The coupling model and geometry applicable to a two-layer Ni–Fe/Mn–Ir film is shown schematically in Fig. 1. The ferromagnetic and antiferromagnetic layers have thicknesses d_F and d_{AF}, respectively. The orientation angles for the in-plane magnetic field H, the ferromagnetic film magnetization vector, and the antiferromagnetic spin axis are shown as θ,
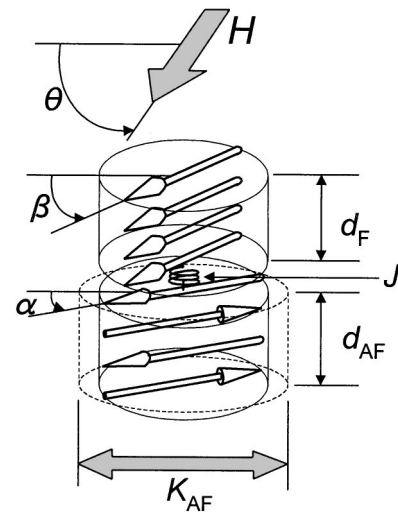

FIG. 1. Schematic diagram of the magnetic bilayer structure used for the exchange anisotropy model calculations. The spin moments in the ferromagnetic (F) layer of thickness d_F and the antiferromagnetic (AF) layer of thickness d_{AF} are indicated as open arrows. The exchange coupling at the interface is indicated by the spring labeled J. The uniaxial anisotropy for the AF layer is indicated by the large shaded arrow labeled K_{AF} and elongated dashed line cylinder. The shaded arrow H denotes the applied in plane magnetic field. The orientations of the various vector components are given by the angles α, β, and θ, as indicated.

α, and β, respectively. The small spring labeled J indicates the interface exchange coupling. The layers are assumed to have in-plane spins only, and no domains. The uniaxial anisotropy axis for the antiferromagnetic layer is indicated by the shaded arrow labeled K_{AF}. No magnetic anisotropy has been taken into account for the ferromagnetic layer in this model, to observe the unique effect of exchange interaction between the ferromagnet and the antiferromagnet on macroscopic magnetization, magnetic torque curves and rotational hysteresis losses.

Following Ref. 6, one may write the total free energy per unit surface area as tE, where t is the total film thickness and E is an average energy density per unit volume, in the form shown in

$$tE = -M_s d_F H \cos(\theta - \beta)$$
$$+ K_{AF} d_{AF} \sin^2 \alpha - J \cos(\beta - \alpha). \quad (1)$$

In Eq. (1), M_s denotes the saturation magnetization per unit volume of the ferromagnetic layer, K_{AF} is the uniaxial anisotropy constant in units of energy per unit volume for the antiferromagnetic layer, and J is the exchange coupling energy per unit area of the interface between the layers. The ferromagnetic layer is taken to be isotropic. From the usual energy minimization procedure, one obtains the following conditions for static equilibrium:

$$(K_{AF} d_{AF}/J) \sin 2\alpha = \sin(\beta - \alpha), \quad (2)$$

$$(M_s d_F H/J) \sin(\theta - \beta) = \sin(\beta - \alpha). \quad (3)$$

Keep in mind that in the experiment, the control parameters are the antiferromagnetic Mn–Ir layer thickness d_{AF}

and the applied magnetic field H. For the analysis, it will prove convenient to define a reduced d_{AF} control parameter C_{dAF} according to

$$C_{dAF} = K_{AF} d_{AF}/J, \tag{4}$$

and a reduced field control parameter C_H according to

$$C_H = M_s d_F H/J. \tag{5}$$

For the model calculations, Eqs. (2) and (3) were solved numerically for the magnetic moment orientation angles α and β as a function of C_{dAF}, C_H, and the field angle θ. These angle results were then used to compute torque curves, magnetization curves, hysteresis loops, and related properties for comparison with the experimental data. The significance of C_{dAF} and C_H as control parameters for changes in the magnetic response of the ferromagnetic-antiferromagnetic bilayer films will be apparent from the results given below and the later comparisons with the data.

Some representative results on the basic calculations are shown in Fig. 2. Figure 2(a) shows a constant energy contour plot of β versus α with contour lines for stepped values of a reduced energy parameter tE/J. For this plot, the field angle θ was set at a value slightly greater than 180°, 1.029π, and the C_{dAF} and C_H parameters were set at 0.8 and 0.72, respectively. The reason for this special choice for θ will become clear shortly. For this choice of parameters, there are two minimum energy points as indicated by the crosses at points B and C in the diagram. There is also a submerging stable point at A to be considered shortly. There is a relatively small energy barrier between points A and C which is close to an (α,β) position of $(0.3\pi,0.6\pi)$.

Note that the energy minimum at point A starts out at $\alpha=0$ and $\beta=0$ for $\theta=0$ and moves to the point indicated at $\theta=1.029\pi$. For the indicated C_{dAF} and C_H values, the stability point at A ceases to exist if θ is increased above 1.029π and the stable angle pair (α,β) transits to *a new minimum energy point* at B. The difference in energy which occurs from A to B as θ increases above 1.029π, therefore, is released irreversibly. With further increase in θ, the (α,β) point at B gradually moves to $(2\pi,2\pi)$.

The graphs in Figs. 2(b) and 2(c) clarify the effects demonstrated above. Figure 2(b) shows the variations in the spin angles α and β as a function of the field angle θ for the same C_{dAF} and C_H as used for Fig. 2(a). Figure 2(c) shows the corresponding forward and reverse torque curve responses for increasing and decreasing field angles. The vertical axis in (c) corresponds to tL/J, where L is the torque per unit volume, the tL product denotes the torque per unit film area, and the J divisor provides a normalization to the interface exchange. In Fig. 2(b), the jump in α and β as θ exceeds the 1.029π point discussed above is clear. In Fig. 2(c), the one-fold unidirectional torque character and the presence of rotational hysteresis loss are also clear.

Two types of computed results were obtained from the model analysis. (1) Easy axis magnetization versus field curves and hysteresis loops were obtained from the evaluation of the magnetization component along the unidirectional axis for a bipolar variation in the field parameter C_H at θ $=0$. (2) Torque response curves were evaluated from the
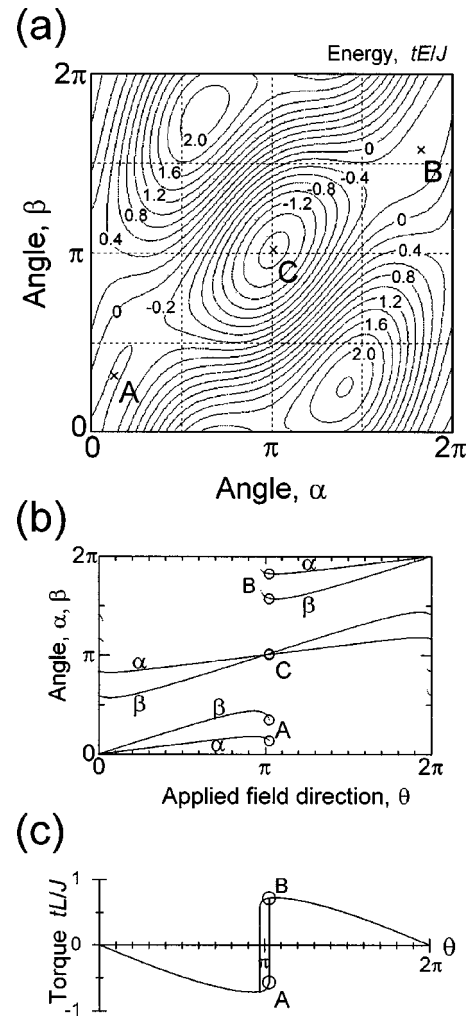

FIG. 2. (a) Contour map of the reduced energy per unit film area as a function of the antiferromagnetic (AF) layer spin axis angle α and the ferromagnetic (F) layer moment angle β. The energy is given in units of tE/J, where E is the energy density, t is the bilayer thickness, and J is an interface exchange coupling parameter. The specific contours were obtained for an AF layer thickness d_{AF} specified by $C_{dAF} = K_{AF} d_{AF}/J = 0.8$, where K_{AF} is the uniaxial anisotropy energy density for the AF layer, and an in-plane field H specified by $C_H = M_s d_F H/J = 0.72$, where M_s and d_F denote the magnetization and thickness of the F layer, respectively. The field was set an angle θ of 1.029π to the uniaxial AF axis. Points B and C denote stable points. Point A denotes a submerging stable point which will disappear for a slight increase in θ. (b) Plots of the stable point angles α and β as a function of the field angle θ for the same thickness and field parameters as in (a). Points A, B, and C are the same as in (a). (c) The torque response is given in units of tL/J, where L is the torque per unit volume, which corresponds to the angle variations in (b).

condition $L(\theta) = -\partial E/\partial\theta$, based on the (α,β) pair solutions as a function of θ for various choices of C_{dAF} and C_H. From the torque results, the $\sin\theta$ and $\sin 2\theta$ torque components were obtained by Fourier analysis and rotational hysteresis loss was obtained as half the area enclosed by the full rotation torque curves obtained for increasing and decreasing θ.

B. Experiment

The samples were prepared under the extremely clean sputtering process conditions described in Ref. 13. The films

were fabricated on silicon wafers with a thermally oxidized layer. These substrates were held at room temperature for the deposition. A specialized rf magnetron sputtering machine was used. The system has four individual sputtering chambers, each with a vacuum capability down to 8×10^{-12} Torr and separation from the main handling chamber by an ultrahigh vacuum (UHV) compatible gate valve. The handling chamber contained a UHV compatible handling robot. The films consisted of four layers, an initial 50-Å-thick tantalum underlayer followed by a 50-Å-thick Ni–Fe ferromagnetic layer, the Mn–Ir antiferromagnetic layer, and a final 50-Å-thick capping layer of tantalum. The thickness of the Mn–Ir layer, denoted by d_{AF}, ranged from 20 to 200 Å. This thickness was controlled through a variation in the layer deposition time which was controlled in turn by mechanical shutters. The Ni–Fe layer composition was 79 wt. % Ni and 21 wt. % Fe. The Mn–Ir layer composition were 74 at. % Mn and 26 at. % Ir. The deposition rates were 1.7 and 0.064 Å/s for the Ni–Fe and the Mn–Ir layers, respectively. Ultraclean argon gas was used for the process gas.[13] The gas pressure during deposition was 0.75 mTorr for the Ni–Fe layer and 20 mTorr for the Mn–Ir layer. A magnetic field of 30 Oe was applied parallel to the plane of the film during the deposition of both the Ni–Fe layer and the Mn–Ir layer. This field direction defines the common antiferromagnetic alignment axis K_{AF} and the reference axis for the measurement field orientation angle θ indicated in Fig. 1.

All measurements were performed at room temperature for the as-deposited films. There was no post deposition heat treatment or other processing. The film microstructure was examined by x-ray diffraction (XRD) with a Co $K\alpha$ radiation source and by transmission electron microscopy (TEM). Magnetization curves and hysteresis loops were measured by vibrating sample magnetometer (VSM) techniques. For the VSM measurements, external magnetic fields up to 2500 Oe were applied along the K_{AF} axis at $\theta=0$ or $\theta=\pi$ according to the convention in Fig. 1. Determinations of the magnetic anisotropy and the rotational hysteresis loss were made from measurements of torque as a function of the in-plane field angle θ for fixed applied fields from 0 to 15 kOe. These data were obtained with a standard null method torque magnetometer with a sensitivity of about 1×10^{-3} dyne cm.

Figure 3 shows a representative hysteresis loop of the net film magnetic moment m versus the bipolar applied field H for a film with a 50 Å thick Mn–Ir layer. It is to be emphasized that these data and all magnetization curve data which follow are for fields applied along the unidirectional axis defined by the deposition field. The data in Fig. 3 demonstrate the displaced loop character produced by the unidirectional exchange anisotropy as well as the usual hysteresis. The exchange anisotropy field H_{ex} indicated in the figure provides a quantitative measure of the interface exchange coupling. The usual coercive field or coercivity H_c is defined as one-half the width of the hysteresis loop at the $m=0$ points of zero moment. These parameters will provide a useful point of comparison between data and theory. The hysteresis loop and torque data will be considered in detail in the Sec. III B.
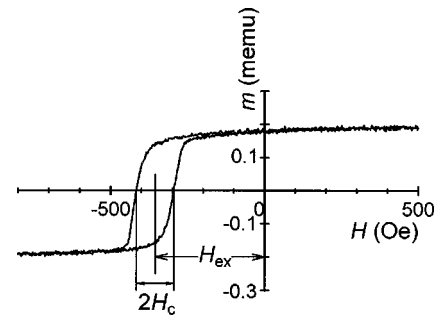

FIG. 3. Typical measured bilayer magnetization curve of the magnetic moment m vs the in-plane magnetic field H. These specific data are for an antiferromagnetic Mn–Ir layer thickness of 50 Å with the magnetic field applied along the antiferromagnetic easy axis. The width of the hysteresis loop is labeled as $2H_c$, where H_c is the coercivity. The shift of the loop is indicated by the exchange anisotropy field H_{ex}.

III. RESULTS

A. Model calculation

Figure 4 shows a series of calculated magnetization curves for fields applied along the $\theta=0$ direction. The vertical axis for each graph shows the component of the ferromagnetic film magnetization along the unidirectional axis, normalized to the saturation magnetization M_s. The horizontal axis on each graph shows the reduced field parameter
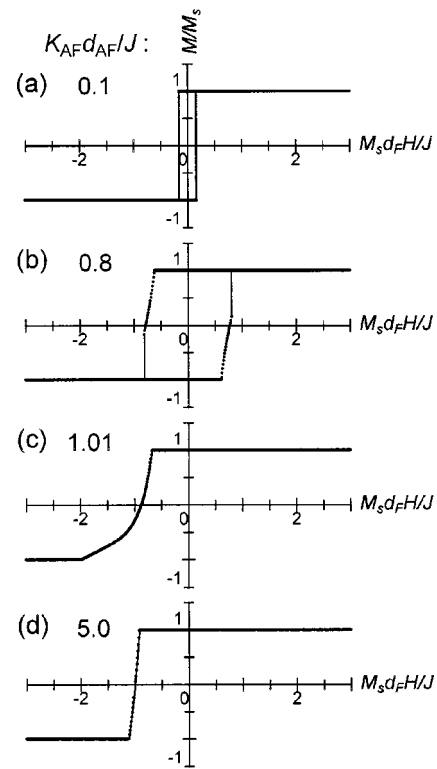

FIG. 4. Calculated magnetization curves of the magnetization M normalized to the saturation magnetization M_s as a function of the in-plane field H. The field axis is given in terms of a reduced field parameter $C_H = M_s d_F H/J$, where d_F is the thickness of the ferromagnetic layer and J is the interface exchange coupling parameter. Graphs (a)–(d) are for increasing values of the antiferromagnetic (AF) layer thickness d_{AF} expressed in terms of a reduced thickness parameter $C_{dAF} = K_{AF} d_{AF}/J$, where K_{AF} is the uniaxial anisotropy energy density for the AF layer.
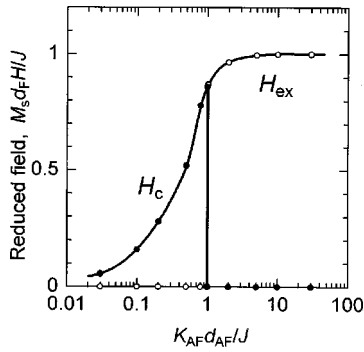
FIG. 5. Exchange anisotropy field H_{ex}, shown as open circles, and the coercivity, H_c, shown as solid circles, as a function of the antiferromagnetic (AF) layer thickness d_{AF}, as obtained from the exchange anisotropy model. The vertical field axis is given in terms of the reduced field parameter $C_H = M_s d_F H/J$, where M_s and d_F denote the magnetization and the thickness of the ferromagnetic layer, respectively, and J is the interface exchange coupling parameter. The horizontal thickness axis is given in terms of the reduced thickness parameter $C_{dAF} = K_{AF} d_{AF}/J$, where K_{AF} is the uniaxial anisotropy energy density for the AF layer.

introduced in Sec. II, $C_H = M_s d_F H/J$. The four graphs show magnetization curves for four values of the Mn–Ir thickness parameter, $C_{dAF} = K_{AF} d_{AF}/J$. These computed curves demonstrate the utility of the C_{dAF} parameter. When C_{dAF} is much smaller than unity, as in graph (a), the computed magnetization curves show a small coercivity and *no* exchange anisotropy shift. If C_{dAF} is increased but kept below unity, as in graph (b), one finds an increase in the coercivity but no exchange anisotropy shift. However, as C_{dAF} is increased above unity, as in (c) and (d), one observes two effects, (i) a disappearance in the hysteresis and (ii) the emergence of a loop shift indicative of exchange anisotropy.

Figure 5 shows the variation in H_c and H_{ex} with the C_{dAF} parameter $K_{AF} d_{AF}/J$ in more detail. The vertical axis shows the model H_c and H_{ex} fields in terms of the reduced field parameter $C_H = M_s d_F H/J$. From this graph, one can see the limiting value of C_H of unity for H_{ex} in the limit of very

large values for C_{dAF} and, hence, for d_{AF}. These results also show that the transition between H_c and H_{ex} occurs at a critical thickness value for d_{AF}, taken as d_{AF}^{cr}, which may defined by $C_{dAF}^{cr} = K_{AF} d_{AF}^{cr}/J = 1$. This simple example demonstrates the physical significance and utility of the C_H and C_{dAF} parameters. The condition $C_H = 1$ yields the upper limit on the exchange anisotropy field. The condition $C_{dAF} = 1$ defines the critical antiferromagnetic layer thickness for the vanishing of hysteresis and the appearance of exchange anisotropy.

Turn now to the evolution in the model torque curve responses as a function of C_H and C_{dAF}. Figure 6 shows five panels of five torque curves each. Each torque curve is in the same format as in Fig. 2(c). The five panels, (a)–(e), reflect the effect of a systematic change in the $C_{dAF} = K_{AF} d_{AF}/J$ thickness parameter, as shown. The graphs in each panel are for systematic changes in the $C_H = M_s d_F H/J$ field parameter, as indicated. First consider panel (a) for $C_{dAF} = 0.1$. In this limit, d_{AF} is well below the d_{AF}^{cr} value introduced above. The graphs in (a) show that in this limit, the torque curve exhibits a basic unidirectional $\sin\theta$ character at low field ($C_H = 0.05$) which evolves into a $\sin 2\theta$ characteristic at high field ($C_H = 0.4$). Rotational hysteresis loss appears suddenly when C_H exceeds 0.1 and then decreases gradually and vanishes at high fields. At $C_{dAF} = 0.1$, the $C_H = 0.1$ point represents a critical field for the vanishing $\sin\theta$ character and for the appearance of rotational hysteresis loss. The critical field value for H is taken as H_{cr}, which may defined by $C_H^{cr} = M_s d_F H_{cr}/J = 0.1$ for this case. The situation is similar for panel (b) and $C_{dAF} = 0.5$. Now, however, the critical field C_H^{cr} has increased and corresponds to $C_H = 0.5$. For panel (c) and the critical thickness point at $C_{dAF} = 1$ noted above, the torque response becomes more complicated. While the torque response still has a $\sin\theta$ character at low field and a $\sin 2\theta$ characteristic at high field, the onset of rotational hysteresis occurs for relatively low fields ($C_H = 0.9$) and persists up to very high fields ($C_H > 10$). When d_{AF} exceeds d_{AF}^{cr} and
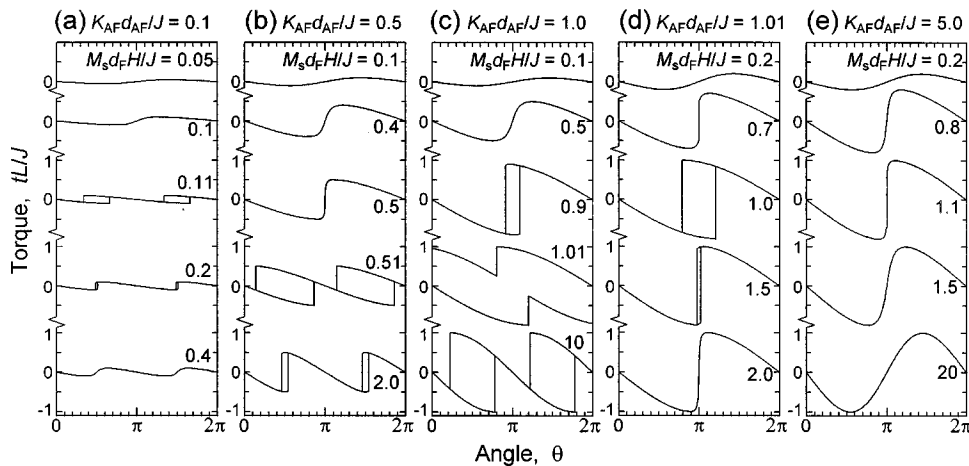

FIG. 6. Computed torque curves from the exchange anisotropy model. The vertical axes show the torque per unit volume L in units of tL/J, where t is the bilayer thickness, and J is the interface exchange coupling parameter. The field angle θ on the horizontal axis is referenced to the antiferromagnetic (AF) easy axis. Panels (a) through (e) are for increasing values of the AF layer thickness d_{AF}, expressed in terms of $C_{dAF} = K_{AF} d_{AF}/J$, where K_{AF} is the uniaxial anisotropy energy density for the AF layer. The individual graphs in the panels are for different values of the in-plane field H, expressed in terms of $C_H = M_s d_F H/J$, where M_s and d_F denote the magnetization and the thickness of the ferromagnetic layer, respectively.
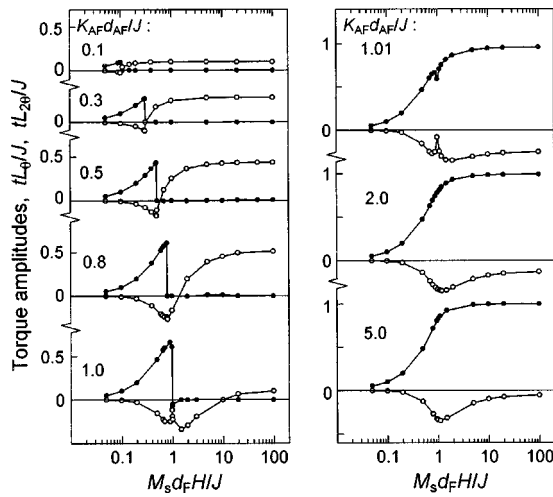
FIG. 7. Torque Fourier amplitudes L_θ and $L_{2\theta}$ for the $\sin\theta$ and $\sin 2\theta$ torque components, respectively, vs field. These were obtained from computed torque curves similar to those in Fig. 6. The vertical scales give the amplitudes in units of $tL_{\theta,2\theta}/J$, where t is the bilayer thickness and J is the interface exchange coupling parameter. The horizontal axes show the in-plane field H in terms of $C_H = M_s d_F H/J$, where M_s and d_F denote the magnetization and the thickness of the ferromagnetic layer, respectively. The solid and open circles show the $\sin\theta$ and $\sin 2\theta$ torque component coefficients, respectively, where the field angle θ is referenced to the anti-ferromagnetic (AF) easy axis. The eight graphs are for increasing values of the AF layer thickness d_{AF}, expressed in terms of $C_{dAF} = K_{AF} d_{AF}/J$, where K_{AF} is the uniaxial anisotropy energy density for the AF layer.
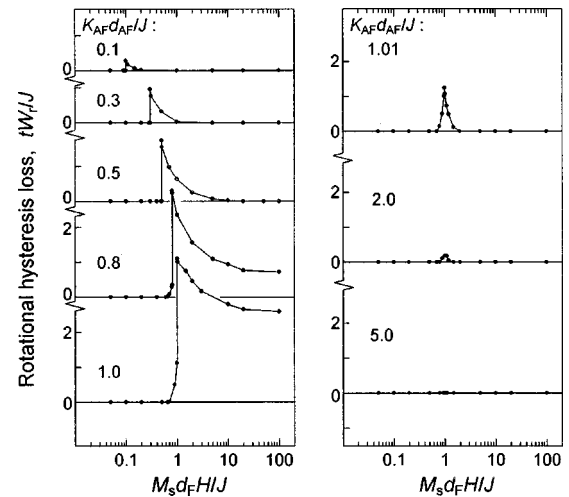
FIG. 8. Rotational hysteresis loss vs field for computed torque curves similar to those in Fig. 6. The vertical axes give the loss in terms of tW_r/J, where W_r is the rotational hysteresis energy loss per cycle per unit volume, t is the bilayer thickness, and J is the interface exchange coupling parameter. The loss was obtained as one-half the area enclosed between forward and reverse torque curves. The horizontal axes show the in-plane field H in terms of $C_H = M_s d_F H/J$, where M_s and d_F denote the magnetization and the thickness of the ferromagnetic layer, respectively. The eight graphs are for increasing values of the AF layer thickness d_{AF}, expressed in terms of $C_{dAF} = K_{AF} d_{AF}/J$, where K_{AF} is the uniaxial anisotropy energy density for the AF layer.

C_{dAF} exceeds unity, as in (d) and (e), the evolution in the torque character with field changes drastically. Even in the case $C_{dAF} = 1.01$ for the second from the right panel where d_{AF} is slightly above d_{AF}^{cr}, all of the torque curves show a $\sin\theta$ character up to the highest fields. Here, moreover, rotational hysteresis appears close to the $C_H = 1$ point and vanishes at high field. For panel (e) and $C_{dAF} = 5.0$, one has a $\sin\theta$ character for all fields and there is no rotational hysteresis for any field.

Figures 7 and 8 show further details on the evolution in the torque response for a wide range of values for the thickness parameter C_{dAF} and the field parameter C_H. The eight graphs in Fig. 7 show the Fourier amplitudes L_θ and $L_{2\theta}$ for the $\sin\theta$ and $\sin 2\theta$ torque components, respectively. The solid circles are for L_θ and the open circles are for $L_{2\theta}$. These amplitudes were obtained from computed torque curves similar to those in Fig. 6. The vertical axes in these graphs show the torque coefficients in the same normalized tL/J units as in Figs. 2 and 6. The graphs in Fig. 8 show companion results on the rotational hysteresis. The vertical axes for these graphs show the results in terms of tW_r/J, where W_r is the rotational hysteresis energy loss per cycle per unit volume. The energy loss was obtained as one-half the area enclosed between forward and reverse torque curves. The results in both figures are for torque components or rotational hysteresis as a function of C_H over the range $0.01 < C_H < 100$ and with individual graphs for values of C_{dAF} from 0.1 to 5.0.

These model calculations demonstrate quite remarkably the changes in the character of the magnetic torque response which take place at the transition points $C_{dAF} = 1$ and C_H

$= C_H^{cr}$. As long as the AF layer thickness is such that $C_{dAF} \leq 1$ is satisfied, for example, the $\sin\theta$ torque component is positive and increasing while the $\sin 2\theta$ component is negative and increasing. Precisely at $C_H = C_H^{cr}$, the $\sin\theta$ torque clamps to zero. At the same time, the $\sin 2\theta$ component begins an upward transition to positive values which saturate close to the maximum value of the $\sin\theta$ torque for large values of C_H. It should be noticed that the value of the reduced critical field C_H^{cr} agrees with the value of the thickness parameter C_{dAF} in every case for which the condition $C_{dAF} \leq 1$ is satisfied, as shown in the left side graphs of Fig. 7. The significance of this correspondence between C_H^{cr} and C_{dAF} will be apparent from the later comparisons with data. When C_{dAF} exceeds unity, the character of both components of the torque change drastically, as shown in the right side graphs of Fig. 7. The companion changes in the rotational hysteresis at the $C_{dAF} = 1$ and $C_H = C_H^{cr}$ points are also clear from Fig. 8.

The results from the model calculations shown above agree with the qualitative description of the rotational hysteresis process given by Jacobs and Bean.[16] First consider the limit of a very thin AF layer. When an antiferromagnetic anisotropy is much smaller than an exchange anisotropy coupling (*in the present words*, $C_{dAF} = K_{AF} d_{AF}/J \ll 1$ is satisfied), the axis of magnetization of the antiferromagnetic layer follows close to the magnetization of the ferromagnetic layer, which is rotating with the large applied field. Owing to the uniaxial anisotropy of the antiferromagnetic layer, the whole system takes on the behavior, exhibiting a nonshifted magnetization curve and a $\sin 2\theta$ torque function without rotational hysteresis loss.
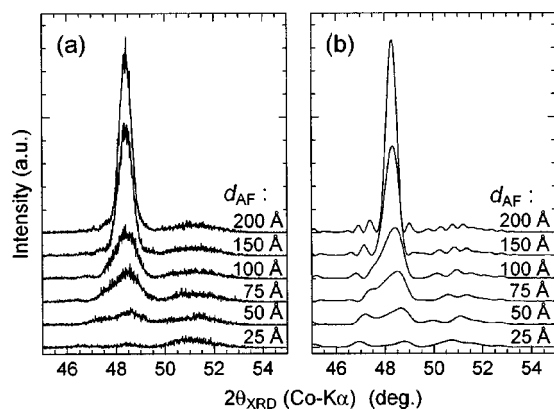
FIG. 9. Graphs (a) and (b) show measured and calculated x-ray diffraction intensity vs angle profiles for typical films. The individual curves are for different values of the antiferromagnetic layer thickness d_{AF}, as indicated. The ''$2\theta_{XRD}$ (Co $K\alpha$)'' label on the horizontal axis refers to the scattering angle for the Co $K\alpha$ radiation.

Now consider critical thickness point discussed above. When the antiferromagnetic anisotropy and the exchange-anisotropy coupling are comparable ($C_{dAF} = K_{AF} d_{AF}/J \approx 1$ is satisfied), the axis of magnetization of the antiferromagnetic layer departs from its original easy direction, but more slowly than the magnetization of the ferromagnetic layer. At a critical angle, this antiferromagnetic axis changes abruptly and irreversibly to a new position lying close to the new easy configuration described by a 180° reversal of all atomic moments in the antiferromagnetic layer. The system has two easy directions, i.e., it does not exhibit the unidirectional anisotropy at the same time as it develops rotational hysteresis losses.

Finally, consider the case in which the thick AF layer. When the antiferromagnetic anisotropy is much larger than the exchange-anisotropy coupling ($C_{dAF} = K_{AF} d_{AF}/J \gg 1$ is satisfied), the magnetization of the ferromagnetic layer follows the large rotating applied field, making small reversible excursions about its direction. The axis of magnetization of the antiferromagnetic layer also makes small reversible excursions about its preferred direction. There is no rotational hysteresis but there is unidirectional anisotropy manifested by a shifted magnetization curve (nonhysteretic) and a $\sin\theta$ torque function.

B. Experimental results

1. Film microstructure

Figure 9 shows measured and calculated x-ray diffraction profiles for a series of films with different AF layer thickness d_{AF} values. The data are shown in (a). Calculated profiles are shown in (b). The calculations were done through the use of a step model.[17,18] For these calculations, the film was taken to consist of a substrate with a 50 Å β-Ta layer, a 50 Å fcc Ni–Fe layer, an fcc $Mn_{75}Ir_{25}$ layer of thickness d_{AF} as indicated, and a final 50-Å-thick β-Ta capping layer. The Ni–Fe and Mn–Ir layers were taken to be disordered. The lattice relationship between the substrate surface and the respective layers was taken to be substrate/Ta (002)/Ni–Fe (111)/Mn–Ir (111). The lattice spacings used for the
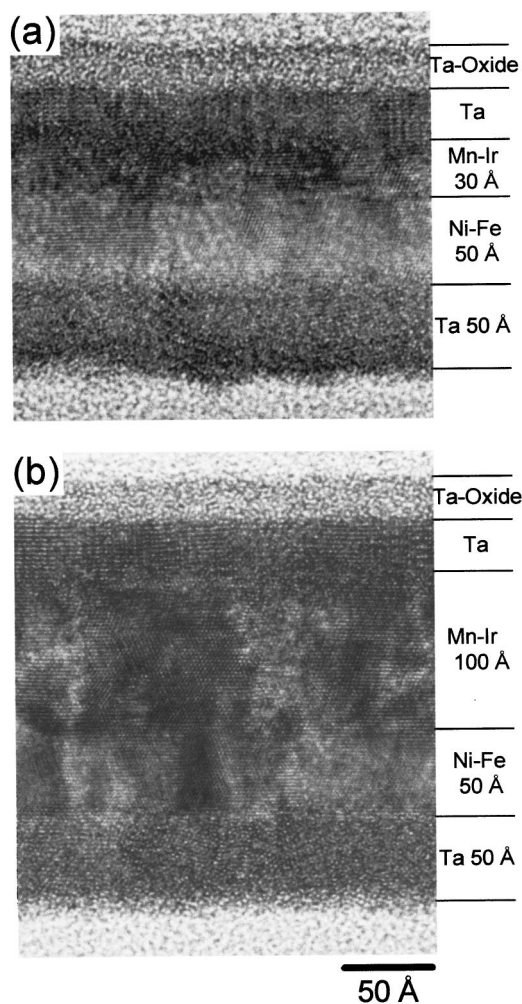

FIG. 10. Typical cross-section transmission electron microscopy images for the films. Images (a) and (b) are for nominal antiferromagnetic layer thickness values of 30 and 100 Å, respectively.

calculations were 2.658 Å for the tantalum, 2.055 Å for the Ni–Fe, and 2.188 Å for the Mn–Ir. One can see good agreement between the measured and the calculated profiles. This agreement indicated that the films consist of highly coherent crystal planes which are stacked parallel to the film plane and that the thickness of the AF Mn–Ir layer in each case is uniform and accurate.

In order to clarify the microstructure of the AF layer, film cross sections were observed by TEM. Figure 10 shows typical TEM images for the film cross sections. The images in (a) and (b) are for nominal Mn–Ir thickness values of 30 and 100 Å, respectively. These images show that the AF layers consist of highly oriented fcc-(111) crystal planes which extend from the Ni–Fe layer to the top of the Mn–Ir layer. This uniform layer structure is consistent with the good agreement between the measured and calculated XRD profiles in Fig. 9. The TEM data also show that the AF layer thickness is highly uniform. The fluctuation in d_{AF} over the scale of the images in Fig. 10 is less than a few monolayers. The images also show evidence for grain boundaries perpendicular to the film plane. This indicates a columnar microstructure for the Ni–Fe/Mn–Ir bilayers in which Mn–Ir
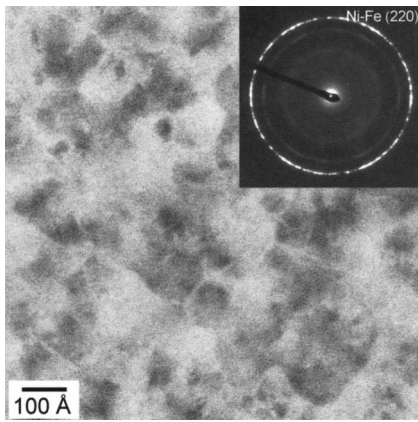
FIG. 11. Typical top view transmission electron microscopy image for a 50 Å Ni–Fe layer deposited on the Ta layer. The inset shows the corresponding electron diffraction pattern for the film.

grains which form the AF layer grow on the underlying Ni–Fe grains by epitaxy.

Figure 11 shows a top view TEM image and an electron diffraction pattern for a 50-Å-thick Ni–Fe layer on the Ta underlayer. One can see Ni–Fe grains which are about 100 Å in diameter. The random two-dimensional (2D) texture shows that there is no clear preferred orientation in the film plane. Given the evidence for epitaxy of the Mn–Ir on the Ni–Fe from Fig. 10, one may conclude that this random 2D texture applies to the complete Ni–Fe/Mn–Ir bilayer film.

2. Hysteresis loop response

Figure 12 summarizes the results of hysteresis loop measurements for films with a range of d_{AF} values from 20 to 200 Å. The figure shows the variation in the measured exchange coupling field H_{ex} and the coercivity H_c with the antiferromagnetic layer thickness. These data show that H_{ex} becomes nonzero when d_{AF} exceeds about 25 Å, rises rapidly, reaches a peak value of about 370 Oe at $d_{AF} \approx 75$ Å, and then gradually decreases. If the peak in H_{ex} at 370 Oe is combined with the empirical $M_s d_F$ product value of 4.0×10^{-4} emu/cm^2, one obtains a unidirectional anisotropy constant $J_K \equiv M_s d_F H_{ex}$ of 0.147 erg/cm^2. This J_K value is
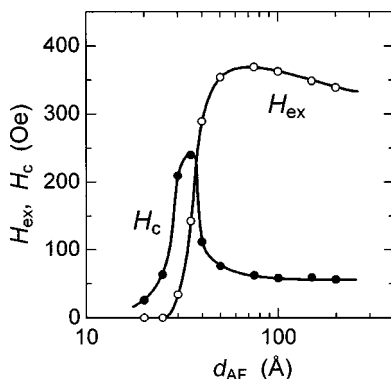

FIG. 12. Exchange anisotropy field H_{ex}, shown as open circles, and the coercivity, H_c, shown as solid circles, as a function of the antiferromagnetic layer thickness d_{AF}, as obtained from the room temperature hysteresis loop measurements.

comparable to previously reported values.[19] The coercivity H_c, on the other hand, show a peak response. The coercivity is 26 Oe at $d_{AF} = 20$ Å, increases to a peak value of 240 Oe at $d_{AF} \approx 35$ Å, and then decays rapidly to a nearly constant value of 60 Oe for $d_{AF} \gtrsim 100$ Å or so. Note that the coercivity for a 50-Å-thick Ni–Fe film alone was only about 1 Oe. One can associate the much larger H_c value for the Ni–Fe/Mn–Ir bilayer in the large d_{AF} limit with irreversible spin flopping in the AF layer and/or irreversible pinning of the walls or local spins in the F layer at the F/AF interface.[20,21]

Figure 12 is the experimental counterpart to the model calculation results in Fig. 5. The data provide empirical support for the model exchange anisotropy mechanism and provide a basis for an estimation of the critical AF layer thickness parameter d_{AF}^{cr}. While the match between the H_{ex} and H_c responses in Figs. 5 and 12 is not perfect, there is a qualitative match between two essential features. First, note the near saturation in H_{ex} at large values of d_{AF} in Fig. 12 and the saturation in Fig. 5 for the corresponding reduced field $C_H = M_s d_F H/J$ at $C_H = 1$ for large values of the reduced d_{AF} control parameter $C_{dAF} = K_{AF} d_{AF}/J$. Second, note the sharp peak in H_c at $d_{AF} \approx 35$ Å in Fig. 12 and the maximum in the corresponding C_H value in Fig. 5 at $C_{dAF} = 1$. Recall that the condition $C_{dAF} = 1$ corresponds to a critical value d_{AF}^{cr} for the AF layer thickness for the vanishing of hysteresis and the appearance of exchange anisotropy. One may thus estimate the critical thickness d_{AF}^{cr} as the point in Fig. 12 at which the coercivity drops steeply. This point is taken at $d_{AF} = d_{AF}^{cr} = 37$ Å.

By using this d_{AF}^{cr} value and regarding the maximum experimental value of $J_K = 0.147$ erg/cm^2 as an Ni–Fe/Mn–Ir interface exchange parameter J, the anisotropy constant of the antiferromagnetic layer K_{AF} ($\equiv J/d_{AF}^{cr}$; Ref. 22) is estimated as 4.0×10^5 erg/cm^3.

3. Torque response

Figures 13, 14, and 15 give data on the experimental torque response as a function of the applied in-plane field H and the AF layer thickness d_{AF}. Figure 13 shows actual torque curves. The vertical axes show the torque thickness tL product. The horizontal axes give the in-plane field angle relative to the AF easy axis. Panels (a) through (e) are for the indicated values of d_{AF}. The indicated d_{AF} values 25, 30, 40, 50, and 200 Å correspond to the respective C_{dAF} values 0.68, 0.81, 1.08, 1.35, and 5.4, based on the exchange and anisotropy parameter values obtained above. The torque curves in each panel are for the indicated H values.

The seven graphs in Fig. 14 show the Fourier amplitudes L_θ and $L_{2\theta}$ for the $\sin\theta$ and $\sin 2\theta$ torque components, respectively. The solid circles are for L_θ and the open circles are for $L_{2\theta}$. These amplitudes were obtained from measured torque curves similar to those in Fig. 13. The vertical axes show torque thickness product for these amplitudes. The graphs in Fig. 15 show companion data on the rotational hysteresis. The vertical axes for these graphs show the results in terms of tW_r, where W_r is the rotational hysteresis energy loss per cycle per unit volume. These values were obtained from one-half the area enclosed by torque curves for forward and reverse rotations. In the graphs for Figs. 14 and 15, the
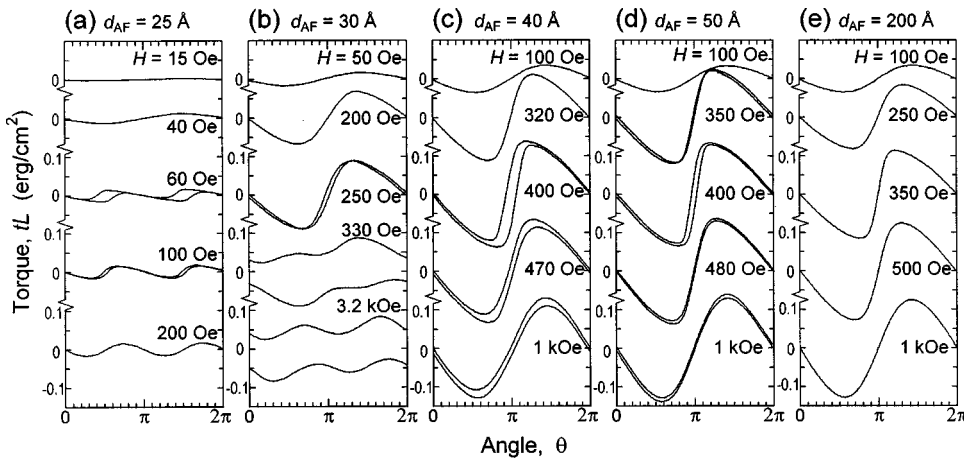
FIG. 13. Measured torque vs field angle for films with a range of antiferromagnetic layer thickness d_{AF} values, as indicated for each panel, and for the indicated values of the applied in-plane magnetic field H. The vertical axis shows the product of the torque per unit volume L and the film thickness t. The horizontal axis shows the in-plane field angle θ relative to the antiferromagnetic easy axis.

horizontal field axis for all the graphs runs from below 10 Oe ($C_H \approx 0.027$) to over 10 000 Oe ($C_H \approx 27$). Here, the corresponding C_H values are obtained from the empirical $M_s d_F$ product value of 4.0×10^{-4} emu/cm² and the exchange parameter obtained above.

The data in Figs. 13–15 exhibit many but not all of the features found in the model calculation results of Figs. 6–8. Except for the data for the lowest Mn–Ir thickness, the indicated d_{AF} values as well as the H values and axis scales in these figures more or less match the corresponding C_{dAF} and C_H parameters in Figs. 6–8. Generally speaking, the experimental torque curves, the $\sin \theta$ and $\sin 2\theta$ torque component response as a function of H, and the rotational hysteresis versus H behavior tend to follow the model. At small d_{AF} values, as in the left two panels of Fig. 13 for example, one finds an evolution in the torque from a $\sin \theta$ response at low field to a $\sin 2\theta$ response at high field. At large d_{AF}, on the other hand, one sees a pure $\sin \theta$ response at very low and

very high fields with a $\sin 2\theta$ component only for intermediate fields.

First consider the experimental data for d_{AF} values below the critical antiferromagnetic layer thickness $d_{AF}^{cr} = 37$ Å.

In the case of $d_{AF} = 25$ Å ($C_{dAF} = 0.68$), the torque curve exhibits the $\sin \theta$ character at low field ($H \leq 40$ Oe) which evolves into a $\sin 2\theta$ characteristic at $H > 40$ Oe. The rotational hysteresis loss also appears at the field higher than 40 Oe and decreases gradually and vanishes at high fields. One can say that these changes of the torque curve response against the applied field qualitatively agree with the MB model calculation for $C_{dAF} \leq 1$. The most remarkable difference of the measured results from the calculated ones is a disagreement of both values of the reduced critical field C_H^{cr} and of the reduced antiferromagnetic layer thickness C_{dAF}, while they should agree with each other in the calculation for $C_{dAF} \leq 1$ cases as mentioned in Figs. 7 and 8. The critical field 40 Oe determined from the experimental results represents $C_H^{cr} = 0.11$, which is quite different from 0.68 of the
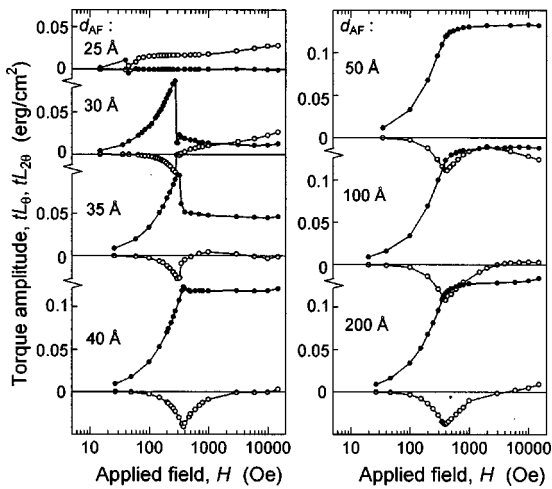

FIG. 14. Torque Fourier amplitudes L_θ and $L_{2\theta}$ for the $\sin \theta$ and $\sin 2\theta$ torque components, respectively, versus field H. These were obtained from measured torque curves similar to those in Fig. 13. The vertical scales give the amplitudes in units of $tL_{\theta,2\theta}$, where t is the bilayer thickness. The solid and open circles show the $\sin \theta$ and $\sin 2\theta$ torque component coefficients, respectively, where the field angle θ is referenced to the antiferromagnetic (AF) easy axis. The seven graphs are for increasing values of the AF layer thickness d_{AF}, as indicated.
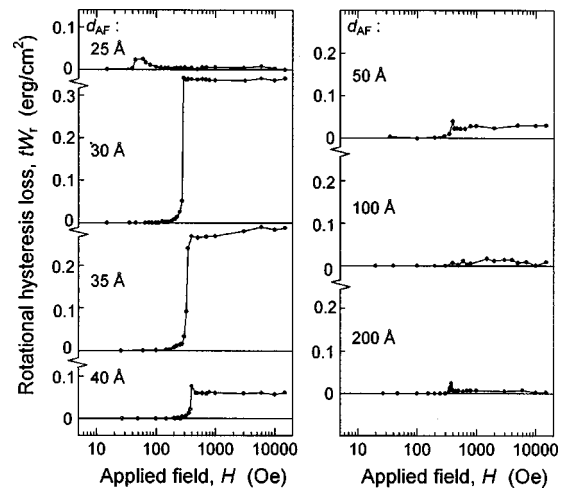

FIG. 15. Rotational hysteresis loss vs the in-plane field H for measured torque curves similar to those in Fig. 13. The vertical axes give the loss in terms of tW_r, where W_r is the rotational hysteresis energy loss per cycle per unit volume and t is the bilayer thickness. The loss was obtained as one-half the area enclosed between forward and reverse torque curves. The seven graphs are for increasing values of the antiferromagnetic layer thickness d_{AF}, as indicated.

value of C_{dAF} in this case. The cause of this disagreement will be discussed in the next section.

When $d_{AF} = 30$ Å ($C_{dAF} = 0.81$), the torque curve exhibits the $\sin\theta$ characteristics in the low field ($H < 290$ Oe) and it changes component to the $\sin 2\theta$ characteristics with increasing field, while a small $\sin\theta$ component remains up to the high field. The rotational hysteresis loss tW_r, which is almost zero in the low field, appears around $H = 200$ Oe and steeply increases to 0.34 erg/cm^2 at $H = 290$ Oe. With further increase of the field, the rotational hysteresis loss remains almost constant. The reduced rotational hysteresis loss tW_r/J is estimated as 2.3 from the constant value of $tW_r = 0.34$ erg/cm^2, by regarding the coupling energy J as the unidirectional anisotropy constant $J_K = 0.147$ erg/cm^2 (maximum experimental value). These changes of the torque curve show some similarities to the calculated results for the case of $C_{dAF} \sim 1$ (Figs. 6–8). That is to say, (1) the rotational hysteresis loss appears even in a onefold symmetry ($\sin\theta$) torque curve region; (2) the steep increase of the rotational hysteresis loss accompanied with the change of the dominant torque component from $\sin\theta$ to $\sin 2\theta$ at the critical field; (3) the good agreement between the values of the reduced critical field $C_H^{cr} = 0.78$ ($H_{cr} = 290$ Oe) and of the reduced antiferromagnetic layer thickness $C_{dAF} = 0.81$; (4) fairly good agreement for the maximum value of the reduced rotational hysteresis loss: $tW_r/J = 2.3$ for the measurement and 3.1 for the calculation in the case of $C_{dAF} = 0.8$; (5) the nonvanishing rotational hysteresis loss up to very high field.

On the other hand, there still exist some disagreements between the calculated and the measured torque curves. Namely, (1) the remaining of nonzero $\sin\theta$ component at the field higher than the critical field; (2) the collapsed shape of the enclosed area of torque curves (hysteresis loss), which is not harmonic and has little angle variation, at very high field ($H = 3.2$ kOe) in Fig. 13, referring the two individual loss areas of the calculated ones (as an example, $C_{dAF} = 1.0$ and $C_H = 10$ in Fig. 6); (3) no decay of the rotational hysteresis loss against the field higher than the critical field. These discrepancies are considered in the next section.

As d_{AF} is increased above the critical antiferromagnetic layer thickness $d_{AF}^{cr} = 37$ Å, the torque data evolve into the response expected from the model calculation in the $C_{dAF} > 1$ case.

In the case of $d_{AF} = 40$ Å ($C_{dAF} = 1.08$), the torque curve exhibits the $\sin\theta$ characteristics under the whole field applied. The magnitude of the $\sin\theta$ component gradually increases with increasing the field up to the critical field of 400 Oe, and saturates to be a value of 0.12 erg/cm^2. This value well corresponds to the unidirectional anisotropy constant of the same film $J_K = 0.11$ erg/cm^2, determined from the magnetization curve. Concerning the shape of torque curves in Fig. 13, a slope around $\theta = \pi$ gradually becomes large with increasing the field up to the critical field $H_{cr} = 400$ Oe. It gradually decreases with further increase of the field. In other words, the magnitude of the $\sin 2\theta$ component with opposite sign to the $\sin\theta$ component reaches a maximum value at the critical field (Fig. 14). The rotational hysteresis loss arises from $H \sim 300$ Oe and steeply increases to 0.08 erg/cm^2 at the critical field; a small value of the rotational hysteresis

loss $tW_r \sim 0.06$ erg/cm^2 still remains up to very high field. One can safely say that these changes of the torque curve are very similar to the calculated results for the case of $C_{dAF} > 1$, except for the nonvanishing hysteresis loss.

In the case of $d_{AF} = 50$ Å ($C_{dAF} = 1.35$), similar changes of the torque curve to the case of $d_{AF} = 40$ Å are observed, however, the remaining rotational hysteresis loss at very high field becomes smaller value, $tW_r \sim 0.03$ erg/cm^2.

For the case of $d_{AF} = 200$ Å ($C_{dAF} = 5.4$), the magnitude of the $\sin\theta$ component gradually increases with increasing the field up to the critical field $H_{cr} \sim 400$ Oe, and slowly approaches to a saturated value of 0.13 erg/cm^2. The $\sin 2\theta$ component and the rotational hysteresis loss appear only in the vicinity of the critical field. From the comparison of these results in Figs. 14 and 15 with the corresponding model calculations for $C_{dAF} = 5.0$ in Figs. 7 and 8, one can say that the model is in *quantitative* agreement with the data in the limit of large d_{AF}. The most important point from these data is the absence of rotational hysteresis loss at high field. This result shows, rather unambiguously, that rotational hysteresis at high field is not an intrinsic characteristic of exchange anisotropy in real system. These results show that F–AF systems with well-defined interfaces and uniform structure confirm to the MB model.

IV. DISCUSSION

The previous section presented detailed data on film microstructure, hysteresis loop characteristics, and the torque response. The MB model calculations of Secs. II A and III A gave a particularly good match to these data in the limit of a large Mn–Ir layer thickness, that is, for $C_{dAF} = K_{AF}d_{AF}/J > 1$. This good match provides an unambiguous answer to previous questions about exchange anisotropy and high field rotational hysteresis loss. The data and the matching results from the model calculations in the $C_{dAF} > 1$ limit clearly show that a rotational hysteresis loss at high field *is not* an essential feature of exchange coupled ferromagnetic and antiferromagnetic systems.

On the other hand, for antiferromagnetic layer thicknesses on the order of the critical thickness, $d_{AF}^{cr} \approx 37$ Å, or smaller, the exchange anisotropy model calculations show significant departures from experiment. Possible reasons for these departures are considered below.

A. Remaining nonzero $\sin\theta$ components at the field higher than the critical field ($d_{AF} = 30$ and 35 Å)

Consider first the problems with the torque data for $d_{AF} = 30$ Å and $d_{AF} = 35$ Å. Notice the data in Fig. 14. The $\sin\theta$ torque component is nonzero and relatively constant in the high field limit, which is larger for $d_{AF} = 35$ Å than for $d_{AF} = 30$ Å. In stark contrast to these results, the model calculations for the corresponding C_{dAF} value show a sharp drop of the $\sin\theta$ torque component to zero when H exceeds the critical field C_H^{cr}. It is proposed that the nonzero $\sin\theta$ torque component in the high field limit for AF films close to the critical thickness is related to local variations in d_{AF}. The data in Fig. 10 revealed such a variation and showed that the films also have a columnar microstructure. It is reasonable to
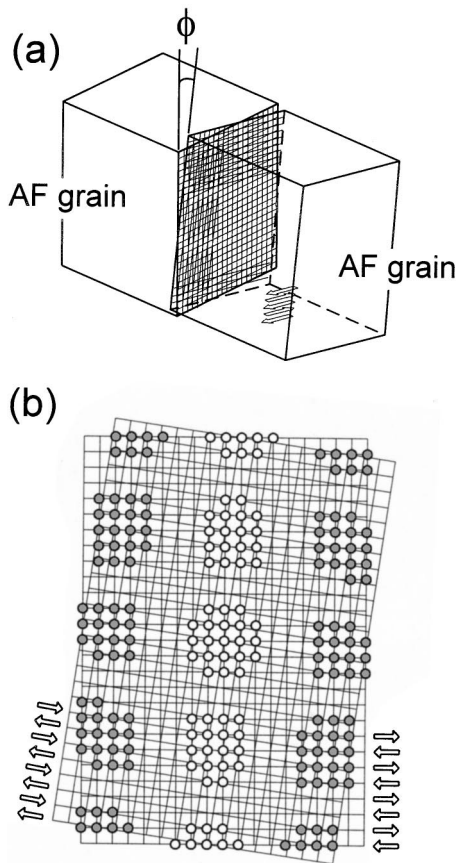
FIG. 16. (a) Schematic model of neighboring antiferromagnetic grains tilted each other by angle ϕ. For simplicity, the grains are treated as rectangular parallelepipeds and antiferromagnetic spins in the grain aligned ferromagnetically in a plane parallel with the bottom. (b) Crystal lattices at the interface are indicated as meshes. The pairs of surface spins of neighboring antiferromagnetic grains which collaborate (compete) with each other are indicated as open (closed) circles.
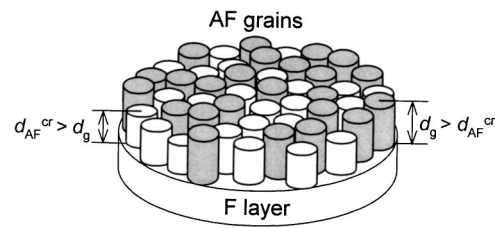

FIG. 17. (a) Schematic model of exchange-coupled ferromagnetic/antiferromagnetic bilayer. The antiferromagnetic layer is regarded as an assemblage of antiferromagnetic grains with respective thickness, d_g. Grains thicker than the critical thickness, d_{AF}^{cr}, contribute to the $\sin \theta$ component of the torque response (shaded grains); thinner ones, to the $\sin 2\theta$ component (white grains).

regard the antiferromagnetic grains as noninteracting. Figure 16(a) represents a schematic model of neighboring antiferromagnetic grains, whose surface spins are compensated at the atomic scale and the crystal lattices of grains are naturally inclining to each other. The pairs of surface spins of the neighboring antiferromagnetic grains thus collaborate or compete with each other at respective parts of the grain boundary through the exchange coupling, when the antiferromagnetic spins reverse in a one-sided grain. In other words, the exchange coupling between the pair of surface spins of the neighboring antiferromagnetic grains are compensated statistically, and the intergranular coupling of antiferromagnetic grains is negligible. This situation is illustrated in Fig. 16(b). An exchange-coupled bilayer with some deviation of the antiferromagnetic layer thickness is now regarded as an assemblage of antiferromagnetic grains with respective thickness, which are exchange coupled with a ferromagnetic layer as shown in Fig. 17. The antiferromagnetic grains with a d_{AF} which is greater than the critical thickness d_{AF}^{cr}, will provide a dominant $\sin \theta$ or onefold torque response which extends to high field as for the bottom left and right side graphs of Fig. 14. The data in Fig. 14 for d_{AF} = 30 Å and d_{AF} = 35 Å show that as the average thickness is increased toward d_{AF}^{cr} = 37 Å, one obtains a *greater* $\sin \theta$

torque component. This response, therefore, is simply a manifestation of the $\sin \theta$ torque component at high field which is found for thick films and a distribution of different d_{AF} within one film.

B. Remaining rotational hysteresis loss at the field higher than the critical field (d_{AF}=40 and 50 Å)

A grain to grain variation in the AF layer thickness also provides a consistent explanation of the persistent rotational hysteresis loss at high field for films close to the critical thickness. Just as an AF layer thickness above the critical thickness produces a high field $\sin \theta$ torque component, an AF layer thickness which is *below* d_{AF}^{cr} produces rotational hysteresis loss. Notice the data in Fig. 15 for d_{AF} = 50 Å. Even though this film has an AF layer which is well above the critical thickness of 37 Å, there is still a residual rotational hysteresis loss which is constant at high field. As one moves to lower AF layer thicknesses in the range of the critical thickness, the proportion of grains with thicknesses *below* d_{AF}^{cr} increases, and the high field rotational hysteresis loss also increases.

C. Disagreement between the values of C_H and C_{dAF} (d_{AF}=25 Å)

Turn now to the problems noted for d_{AF}=25 Å. The transition in the torque from a $\sin \theta$ to a $\sin 2\theta$ character occurs at a much lower field than expected for a d_{AF} value. Conversely, one could say that the value of C_{dAF} needed to explain the data is much too low compared to the actual value of 0.68 obtained from the hysteresis loop data analysis. Thermal effects may provide one possible explanation for this low field threshold change over in the torque character. All of the measurements reported here were made at room temperature. The model calculations, on the other hand, are strictly valid only at 0 K. The energy contour diagram in Fig. 2(a) provides an indication of the effect. As discussed earlier, there is a small energy barrier between the points A and C in Fig. 2(a). The transition from point A to point B yields the $\sin \theta$ torque character evident in Fig. 2(c). Due to the weak barrier from A to C, however, thermal processes can also promote a transition from A to C and produce a $\sin 2\theta$ torque response. This will be possible, therefore, even when C_{dAF} is relatively large and C_H is small.
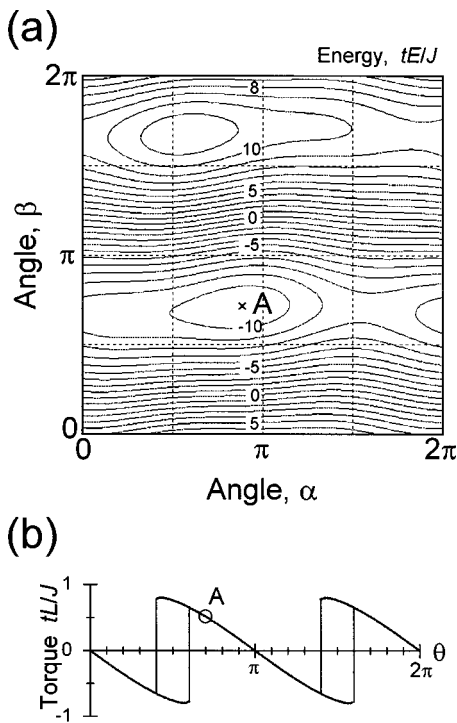
(a)

(b)

FIG. 18. (a) Contour map of the reduced energy per unit film area as a function of the antiferromagnetic (AF) layer spin axis angle α and the ferromagnetic (F) layer moment angle β. The energy is given in units of tE/J, where E is the energy density, t is the bilayer thickness, and J is an interface exchange coupling parameter. The specific contours were obtained for an AF layer thickness d_{AF} specified by $C_{dAF}=K_{AF}d_{AF}/J=0.8$, where K_{AF} is the uniaxial anisotropy energy density for the AF layer, and an in-plane field H specified by $C_H=M_s d_F H/J=10$, where M_s and d_F denote the magnetization and thickness of the F layer, respectively. The field was set an angle θ of 0.7π to the uniaxial AF axis. Point A denotes a stable point. (b) The torque response is given in units of tL/J, where L is the torque per unit volume for the same thickness and field parameters as in (a). Point A is the same as in (a).

Given the possible importance of thermal effects noted above for $d_{AF}=25$ Å, it is tempting to invoke similar processes to explain, at least in part, the effects for the thicker films noted above. On the basis of an energy contour analysis similar to that shown in Fig. 2(a), this does not appear to be the case. Figure 18 shows a calculated energy map at $\theta=0.7\pi$ (a) and a torque curve (b), as an example. The C_{dAF} and C_H parameters were set at 0.8 and 10, respectively. Only one stable solution pair of (α,β) exists at $(0.89\pi,0.72\pi)$ in the energy map.

D. Collapsed shape of the hysteresis loss at very high field ($d_{AF}=30$ and 35 Å)

Finally, we will discuss about the origin of the collapsed shape of the torque response in Fig. 13 for $d_{AF}=30$ Å at very high field. Returning to Fig. 18, one can say that the rotational hysteresis loss should only exist in two individual θ regions under very high applied field as demonstrated in Fig. 18(b) for an example, because the solution pair of (α,β) uniquely exists in other θ regions as demonstrated in Fig. 18(a). Since the hysteresis loss is originated from the antiferromagnetic grains thinner than the critical thickness, the coexistence of thicker antiferromagnetic grains previously
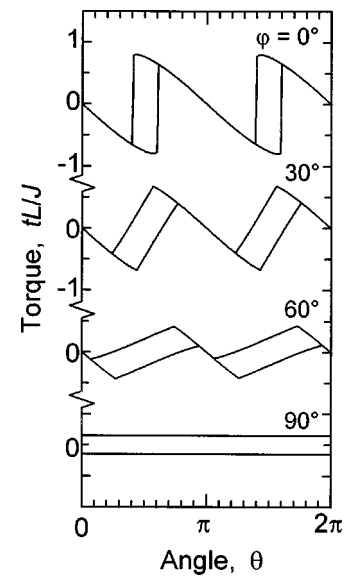

FIG. 19. Computed torque curves from the exchange anisotropy model. The vertical axes show the torque per unit volume L in units of tL/J, where t is the bilayer thickness, and J is the interface exchange coupling parameter. The horizontal axis corresponds to the field angle θ. The AF layer thickness d_{AF} specified by $C_{dAF}=K_{AF}d_{AF}/J=0.8$, where K_{AF} is the uniaxial anisotropy energy density for the AF layer, and an in-plane field H specified by $C_H=M_s d_F H/J=10$, where M_s and d_F denote the magnetization and thickness of the F layer, respectively. The individual graphs are for different values of the distribution angle of the antiferromagnetic (AF) easy axis, φ.

mentioned cannot explain this variance, obviously. One possibility is a distribution of the anisotropy axis of the antiferromagnetic grains in the film plane.

Figure 19 shows the calculated torque curves for $C_{dAF}=0.8$ and $C_H=10$ case, assuming the distribution of the angle of the K_{AF} axis in the film plane. The uniaxial anisotropy (K_{AF}) axes of the antiferromagnetic grains are randomly distributed within $\theta=\pm\varphi$. The shape of enclosed area of the torque curves gradually inclines and the two individual areas tend to be connected to each other with increasing φ. When $\varphi=90°$, which means an isotropic distribution of K_{AF} axes in the film plane, the torque curves naturally become flat. Since the physical origin of K_{AF} used for the calculation is not clear up to the present, we cannot estimate precisely the distribution angle φ in the actual bilayers. If K_{AF} is regarded as magnetocrystalline anisotropy, φ should be 90°, because the columns in the film have no preferred orientation in the film plane as shown in Fig. 11. It is clear that the calculated torque curves for $\varphi=90°$, however, do not correspond with the measurement results. More detailed investigation related to the origin of K_{AF} is required to answer this problem.

The remaining variance between the measurement and the calculation should be discussed is the absence of the decay of the rotational hysteresis loss in the field higher than the critical field in $d_{AF}=30$ and 35 Å cases. Unfortunately, the cause of this variance is not clear at present. One possibility is the distribution of the magnitude of J between each antiferromagnetic grain and the ferromagnetic layer, but this matter requires more detailed study.

J. Appl. Phys., Vol. 87, No. 9, 1 May 2000

Tsunoda *et al.*   4387

V. SUMMARY AND CONCLUSION

Ferromagnetic-antiferromagnetic bilayers were fabricated under the extremely clean sputtering process. These films were used to conduct a critical test of the basic Meiklejohn and Bean (MB) exchange anisotropy model. The films consisted of a Ni–Fe layer for the ferromagnet and a Mn–Ir layer for the antiferromagnet. The Ni–Fe layer thickness was 50 Å for all films. The thickness of the Mn–Ir layer was varied between 20 and 200 Å. The films were deposited in an applied in-plane magnetic field of 30 Oe. The structural properties of the films were determined by x-ray diffraction and transmission electron microscopy. The magnetic properties of the films were determined from hysteresis loop and torque measurements at room temperature.

The film microstructure was highly uniform. The Ni–Fe layers consisted of ordered (111) planes with a random in-plane texture, a columnar microstructure, and grain diameters of about 100 Å. The Mn–Ir layers were highly uniform. These layers had a well-defined (111) orientation relative to the film normal, a random in-plane texture, and the same columnar microstructure as the Ni–Fe underlayer. The Mn–Ir layers had a uniform thickness with a grain-to-grain thickness variation of a few monolayers.

The hysteresis loop data showed a critical antiferromagnetic (AF) layer thickness $d_{AF}^{cr} \approx 37$ Å for the appearance of exchange anisotropy. The film coercive field showed a peak at this thickness and films with thicker AF layers exhibited the shifted hysteresis loops characteristic of exchange anisotropy. Calculations of the coercivity and exchange anisotropy field versus the AF layer thickness based on the MB model were in general agreement with the data. From the critical thickness and the 370 Oe saturation value for the exchange anisotropy field at large AF thicknesses, the model gave values of the interface exchange and the uniaxial anisotropy for the antiferromagnetic layer of 0.147 erg/cm^2 and 4.0×10^5 erg/cm^3, respectively.

The torque data were obtained as a function of the in-plane field angle for fields from 15 Oe to 15 kOe. These data were carefully analyzed to obtain the field dependence of the onefold $\sin\theta$ torque component, the twofold $\sin 2\theta$ torque component, and the rotational hysteresis loss. The torque response could be classified into three categories, based on the thickness of the AF layer. At $d_{AF} = 25$ Å, a thickness somewhat below the critical thickness, the torque exhibited a $\sin\theta$ response at low field which suddenly changed to a $\sin 2\theta$ response for fields above 40 Oe or so. The rotational hysteresis loss also appeared abruptly at 40 Oe, but then decreased with increasing field and vanished for fields above 100 Oe or so.

For films with AF layer thicknesses of 30 and 35 Å, slightly below or nearly equal to the critical thickness, the torque curves, exhibited a $\sin\theta$ response at low fields. At 300–400 Oe, the critical field, this component suddenly dropped to a lower value which remained constant to high field. A small rotational hysteresis loss appeared for fields below the critical value, but increased sharply and saturated for fields above the critical value. The rotational hysteresis persisted up to the highest fields available for measurement, 15 kOe or so.

For d_{AF} values above the critical thickness, the torque showed a predominant $\sin\theta$ response for all fields. The size of this $\sin\theta$ response increased with field and saturated for fields above about 400 Oe. For these films, the $\sin 2\theta$ component of the torque response peaked at 400 Oe and became small at both low and high fields. Rotational hysteresis loss was found around 400 Oe, but the size of this loss was fairly small. For $d_{AF} = 200$ Å in particular, a value well above the critical thickness, the rotational hysteresis loss essentially vanished for fields above 400 Oe.

In general, the hysteresis and torque data could be modeled accurately from the MB exchange anisotropy mechanism. The agreement was particularly good for the thick AF layers. One can conclude from this agreement that a rotational hysteresis loss which persists at high field is not an essential characteristic of exchange anisotropy systems. There were some discrepancies in the details of the torque response from the MB model as compared to the data. Possible origins of these differences include a variation the AF layer thickness from grain to grain, thermal effects because the measurements were all made at room temperature and the MB model shows very small energy barriers between stable states in some cases, and some dispersion in the interface exchange and the AF layer uniaxial anisotropy.

[1] R. D. Hempstead, S. Krongelb, and D. A. Thompson, IEEE Trans. Magn. **MAG-14**, 521 (1978).
[2] B. Dieny, V. S. Speriosu, S. S. P. Parkin, B. A. Gurney, D. R. Wilhoit, and D. Mauri, Phys. Rev. B **43**, 1297 (1991).
[3] W. H. Meiklejohn and C. P. Bean, Phys. Rev. **102**, 1413 (1956); **105**, 904 (1957).
[4] D. Mauri, H. C. Siegmann, P. S. Bagus, and E. Kay, J. Appl. Phys. **62**, 3047 (1987).
[5] A. P. Malozemoff, Phys. Rev. B **35**, 3679 (1987); J. Appl. Phys. **63**, 3874 (1988).
[6] W. H. Meiklejohn, J. Appl. Phys. **33**, 1328 (1962).
[7] D. Paccard, C. Schlenker, O. Massenet, R. Montmory, and A. Yelon, Phys. Status Solidi **16**, 301 (1966).
[8] M. Takahashi, A. Yanai, S. Taguchi, and T. Suzuki, Jpn. J. Appl. Phys., Part 1 **19**, 1093 (1980).
[9] S. Soeya, S. Nakamura, T. Imagawa, and S. Narishige, J. Appl. Phys. **77**, 5838 (1995).
[10] C. H. Lai, H. Matsuyama, R. L. White, T. C. Anthony, and G. G. Bush, J. Appl. Phys. **79**, 6389 (1996).
[11] S. Soeya, H. Hoshiya, M. Fuyama, and S. Tadokoro, J. Appl. Phys. **80**, 1006 (1996).
[12] M. Tsunoda, Y. Tsuchiya, M. Konoto, and M. Takahashi, J. Magn. Magn. Mater. **171**, 29 (1997).
[13] K. Okuyama, T. Shimatsu, S. Kuji, and M. Takahashi, IEEE Trans. Magn. **31**, 3838 (1995).
[14] M. Tsunoda, K. Uneyama, T. Suzuki, K. Yagami, and M. Takahashi, J. Appl. Phys. **85**, 4919 (1999).
[15] K. Hoshino, R. Nakatani, H. Hoshiya, Y. Sugita, and S. Tsunashima, Jpn. J. Appl. Phys., Part 1 **35**, 607 (1996).
[16] I. S. Jacobs and C. P. Bean, in *Magnetism, Vol. III,* edited by G. T. Rado and H. Suhl (Academic, New York, 1963), pp. 323–332.

[17] A. Segmuller and A. E. Blackeslee, J. Appl. Crystallogr. **6**, 19 (1973).

[18] I. K. Schuller, Phys. Rev. Lett. **44**, 1597 (1980).

[19] A. J. Devasahayam, P. J. Sides, and M. H. Kryder, J. Appl. Phys. **83**, 7216 (1998).

[20] V. I. Nikitenko, V. S. Gornakov, L. M. Dedukh, Yu. P. Kabanov, A. F. Khapikov, A. J. Shapiro, R. D. Shull, A. Chaiken, and R. P. Michel, J. Appl. Phys. **83**, 6828 (1998).

[21] H. S. Cho, C. Hou, M. Sun, and H. Fujiwara, J. Appl. Phys. **85**, 5160 (1999).

[22] D. Mauri, E. Kay, D. Scholl, and J. K. Howard, J. Appl. Phys. **62**, 2929 (1987).